Biomaterials 133 (2017) 37–48

Contents lists available at ScienceDirect

Biomaterials

journal homepage: www.elsevier.com/locate/biomaterials

Cell-borne 2D nanomaterials for efficient cancer targeting and photothermal therapy

Zhibin Li [a, b], Jundong Shao [a], Qian Luo [a], Xue-Feng Yu [a, *], Hanhan Xie [a], Haidi Fu [c], Siying Tang [a], Huaiyu Wang [a, **], Guangli Han [c], Paul K. Chu [b, ***]

[a] Institute of Biomedicine and Biotechnology, Shenzhen Institutes of Advanced Technology, Chinese Academy of Sciences, Shenzhen 518055, Guangdong, PR China
[b] Department of Physics and Materials Science, City University of Hong Kong, Tat Chee Avenue, Kowloon, Hong Kong, China
[c] School and Hospital of Stomatology, Wuhan University, 237 Luoyu Road, Wuhan 430079, PR China

ARTICLE INFO

Article history:
Received 27 January 2017
Received in revised form
7 April 2017
Accepted 10 April 2017

Keywords:
2D nanomaterials
Bi_2Se_3 nanosheets
Near-infrared
Drug delivery
Photothermal therapy

ABSTRACT

Two of the challenges for clinical implementation of nano-therapeutic strategies are optimization of tumor targeting and clearance of the nanoagents *in vivo*. Herein, a cell-mediated therapy by transporting 2D Bi_2Se_3 nanosheets within macrophage vehicles is described. The Bi_2Se_3 nanosheets with excellent near-infrared photothermal performance exhibit high macrophage uptake and negligible cytotoxicity thus facilitating the fabrication of Bi_2Se_3-laden-macrophages. Compared with bare Bi_2Se_3, the Bi_2Se_3-laden-macrophages after intravenous injection show prolonged blood circulation and can overcome the hypoxia-associated drug delivery barrier to target the tumor efficiently and dramatically enhance the efficiency of photothermal cancer therapy. The Bi_2Se_3-laden-macrophages possess good biocompatibility as demonstrated by the biochemical and histological analyses and furthermore, most of the materials are excreted from the body within 25 days. Our findings reveal a desirable system for highly efficient near-infrared photothermal cancer therapy.

1. Introduction

Since cancer poses one of the most serious threats to human health, new and more effective therapeutic strategies are demanded and novel nanotechnologies offer the unprecedented opportunity to promote precision treatment of cancer while mitigating undesirable side effects [1–3]. Among the various nano-therapeutic modalities, nanomaterials-mediated photothermal therapy (PTT) which enables localized conversion of tissue-transparent near-infrared (NIR) light into heat to ablate cancer cells has drawn considerable attention [4,5]. Compared to conventional cancer treatment approaches, PTT is minimally invasive, rapid, and easily combined with other therapeutic approaches [6–8]. As a new class of nanomaterials, two-dimensional (2D) nanomaterials are promising PTT agents on account of their intriguing physical and chemical properties [9]. Many types of 2D nanomaterials such as graphene, reduced graphene oxide (rGO), MoS_2, $MoSe_2$, Bi_2Se_3, and black phosphorus (BP) have recently been explored for *in vitro* and *in vivo* PTT of cancer [10–27]. In comparison with other types of PTT agents, 2D nanomaterials generally have large NIR extinction coefficients with little scattering and excellent photothermal stability without undergoing shape transformation upon irradiation with a high-power NIR laser [28]. Moreover, the large surface area of 2D nanomaterials offers plenty of space to engineer a variety of multifunctional nanocomposites suitable for drug delivery and cancer theranostic applications [29–33].

Nanomaterials-mediated cancer therapy generally involves delivery of nanoparticles to the tumor and subsequent light irradiation to produce a high local temperature. It is critical to distribute the nanoparticles evenly at an effective concentration throughout the tumor because nanoparticles cannot functionalize as designed if they do not accumulate at the diseased tissues at a sufficiently high concentration [34–36]. As a common strategy in tumor targeting, the size and surface properties of the nanomaterials are modulated so that they can be passively delivered into tumors by the enhanced permeability and retention (EPR) effect [37,38]. The

* Corresponding author.
** Corresponding author.
*** Corresponding author.
E-mail addresses: xf.yu@siat.ac.cn (X.-F. Yu), hy.wang1@siat.ac.cn (H. Wang), paul.chu@cityu.edu.hk (P.K. Chu).

http://dx.doi.org/10.1016/j.biomaterials.2017.04.012
0142-9612/

biodistribution is governed by several mechanisms including nonspecific binding to proteins in blood, removal by phagocytes, and limitation of the EPR effect which relies on the size, shape, coating, and surface charge of nanomaterials [39]. In this respect, development of new 2D PTT agents is highly desirable in order to improve the tumor-targeting efficiency in cancer therapy.

Since common drugs or nanomaterials delivered in human body often fail to reach many areas, the cell mediated strategy is attractive in therapeutic applications as the nearly impermeable biological barriers can be effectively circumvented [40,41]. Tumor-tropic cells including macrophages [42,43], neural stem cells [44], human CIK cells [45], human induced pluripotent stem cells [46], and mesenchymal stem cells [47] have been proposed as delivery vehicles to transport nanoparticles to tumor tissues. Among them, macrophages with innate phagocytotic capability are attractive as they are circulating cells in human body which can be readily gained [48,49]. It has been reported that macrophages can endocytose Au nanoshells, recognize the cytokines secreted by tumor cells, and migrate to tumor spheroids to produce photothermal effects [50,51]. Recently, our group has produced laden macrophages with gold nanorods and intratumoral injection improves the intratumoral distribution of the nanorods consequently enhancing the photothermal therapeutic efficacy [52]. Nevertheless, in spite of recent advances, there have been few reports on the use of 2D nanomaterial laden macrophages in tumor targeting.

In this work, a cell-borne 2D nanomaterials drug delivery system is designed and produced by loading Bi_2Se_3 nanosheets into macrophages to improve the photothermal therapeutic efficacy. As a member of the 2D layered topological insulators, Bi_2Se_3 nanosheets [53,54] and other bismuth based composites such as MoS_2/Bi_2S_3 [55], MnSe@Bi_2Se_3 [56], and PEG-Bi_2Se_3@PFC@O_2 [57] have recently been demonstrated to be promising tumor imaging or therapy agents delivering high efficiency and multifunctionality. Furthermore, both Se and Bi have excellent biocompatibility and Bi_2Se_3 nanosheets are metabolizable thereby allowing natural clearance from the human body [58]. As shown in Fig. 1, the Bi_2Se_3-laden-macrophages can overcome the hypoxia-associated drug delivery barrier as a “Trojan Horse” delivery vector and infiltrate tumor tissues efficiently. When combined with NIR light irradiation, the strong NIR absorbance of Bi_2Se_3 nanosheets can be exploited to ablate tumor tissues and minimize recurrence.

2. Materials and methods

2.1. Materials

The Dulbecco's modified Eagle's medium and penicillin/streptomycin were obtained from Hyclone Company, South Logan, UT, USA, fetal bovine serum was obtained from Gibco (New York, USA), and near infrared fluorescent dye DIR (KGMP0026) was obtained from Keygen Biotech (China). The other reagents were obtained from Sigma-Aldrich and used without further purification unless mentioned otherwise. Ultrapure water with a resistivity value of about 18.25 MΩ cm^{-1} was obtained from a Milli-Q ion-exchange system (Millipore, USA).

2.2. Synthesis of Bi_2Se_3 nanosheets

The Bi_2Se_3 nanosheets were prepared according to the method described previously [59]. In brief, sodium selenite solution (0.242 g in 35 mL of ethylene glycol) and bismuth nitrate pentahydrate solution (0.452 g in 25 mL of ethylene glycol) were successively added into the poly (vinyl pyrrolidone) solution (PVP, 1.0 g in 40 mL of ethylene glycol) under magnetic stirring at room temperature, by using a 250 mL round-bottom flask as the container. After flask sealing and heating at 160 °C under nitrogen condition, the mixture changed from transparent to milky white and then yellow-white. A hydroxylamine solution (2.4 mL in 20 mL of ethylene glycol) was rapidly injected into the mixture to fabricate Bi_2Se_3 nanosheets. Subsequently, the resultant mixture was cooled down at room temperature, precipitated by centrifuging (12,000 rpm, 10 min), then rinsed three times with a mixture of acetone and D. I. water (300 mL: 60 mL). Finally, the Bi_2Se_3 nanosheets were resuspended in sterile phosphate buffer saline (PBS)

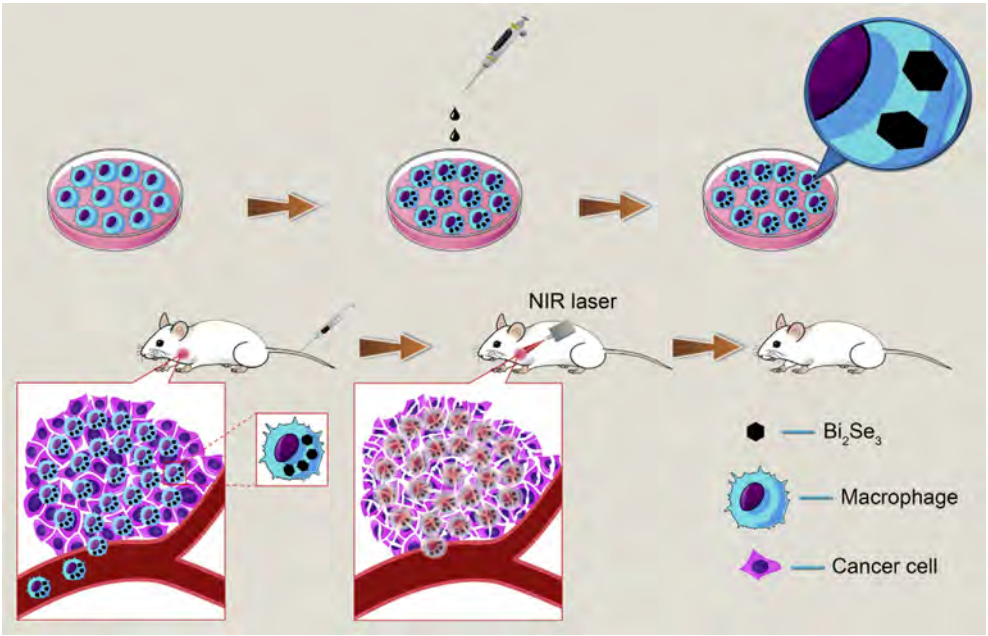

Fig. 1. Schematic illustration of the macrophages loaded Bi_2Se_3 nanosheets delivery system expected to overcome the hypoxia-associated drug delivery barrier to enhance tumor coverage and PTT efficiency.

solution for further performances.

2.3. Characterization

Transmission electron microscopy (TEM) and high-resolution TEM (HR-TEM) were performed on a JEOL JEM-2010 transmission electron microscope at 200 kV and atomic force microscopy (AFM, MFP-3D-S, Asylum Research) was performed in the AC mode (tapping mode) using a nanoprobe (NanoSensors SSS-NCH) with a tip radius as small as 2 nm. The wide-angle X-ray diffraction (XRD) patterns were acquired on the D8 ADVANCE (Bruker) with Cu K_α radiation ($\lambda = 0.1542$ nm) at 40 kV and 40 mA and Energy-dispersive X-ray spectroscopy (EDS) was acquired on the Oxford INCA 300. The concentration of Bi_2Se_3 nanosheets was determined by inductively-coupled plasma optical emission spectrometry (ICP-OES, 7000DV, PerkinElmer) and the UV-vis-NIR absorption spectra were obtained on the TU-1810 spectrophotometer.

2.4. Measurement of Bi_2Se_3 photothermal performance

To assess the photothermal conversion performance of the Bi_2Se_3 nanosheets, a NIR laser (808 nm, 1.0 W/cm^2) was used to irradiate 3 mL of the Bi_2Se_3 nanosheets suspension (5–80 ppm in PBS) in a quartz cuvette until the solution reached a steady-state temperature. The temperature changes were recorded by an infrared thermal imaging camera (Ti27, Fluke).

2.5. Cellular toxicity assay

Both the macrophages (RAW264.7 cells) and breast cancer cells (MCF-7) were cultured in Dulbecco's modified eagle medium supplemented with 10% newborn bovine serum, respectively, in a humidified atmosphere of 5% CO_2 at 37 °C. The cells used in the cellular toxicity assay were initially seeded on a 96-well plate at a density of 1×10^4 cells per well. After culturing for 12 h, the medium was replaced with the culture medium containing different concentrations (2–30 ppm) of Bi_2Se_3 nanosheets and incubated for another 24 h. Afterwards, the cells were rinsed three times with sterile PBS and incubated with 50 μL of the MTT solution (5 mg/mL) for 4 h to form formazan. After dissolving formazan with dimethyl sulfoxide, the optical density of formazan solution was determined spectrophotometrically at 490 nm. The degree of inhibition of cell growth was evaluated by the following formula: Cell viability (%) = (mean of absolute value of treatment group/mean of absolute value of control) × 100%.

2.6. Calcein AM/PI staining

1×10^5 RAW264.7 cells and MCF-7 cells were seeded on the wells of a 24-well plate. After incubation for 12 h, the culture medium was refreshed with the medium containing Bi_2Se_3 nanosheets at different concentrations (15, 20, 25 ppm) and incubated for another 24 h. Afterwards, the cells were washed several times with PBS and co-stained with 50 μg/mL propidium iodide (PI) and 1 μg/mL calcein AM for 15 min. The fluorescence microscopy images were acquired on the Olympus IX71 microscope.

2.7. Flow cytometry

RAW264.7 cells were cultured on a 24-well plate at a density of 1×10^5 cells per well for 12 h then incubated with different concentrations of Bi_2Se_3 nanosheets (15, 20, 25 ppm) for another 24 h. After harvesting, an annexin V-FITC and PI apoptosis detection kit was utilized to stain cells (apoptotic cells were labeled by annexin V-FITC and necrotic cells were labeled by PI) and the labeled cells were further determined by cell Lab Quanta SC flow cytometry (Beckman coulter) to quantify the percentage of apoptotic cells and necrotic cells.

2.8. Cellular uptake of Bi_2Se_3 nanosheets

RAW264.7 cells were cultured on a 24-well plate at a density of 1×10^5 cells per well for 12 h and incubated with different concentrations of Bi_2Se_3 nanosheets (2–25 ppm) for another 24 h. Afterwards, the cells were rinsed with PBS solution three times and the micrographs of Bi_2Se_3-laden-macrophages were acquired on the Olympus IX71 microscope. In the next step, the Bi_2Se_3-laden-macrophages were trypsinized and redispersed in 5 mL of HNO_3 (65%) to dissolve the intracellular Bi_2Se_3 nanosheets after addition of 3 mL of H_2O_2. Subsequently, the mixture underwent 140 °C heating until the solution turned colorless and clear. Finally, the solution after filtering was diluted with deionized water and analyzed by ICP-OES.

2.9. Animal experiments

The athymic BALB/c nude mice and BALB/c mice (5-week old, female) were obtained from Vital River Laboratory Animal Technology Co., Ltd (Beijing, China) and maintained in the animal facility under Specific Pathogen Free (SPF) conditions. The animal study was approved by the Institutional Animal Care and Use Committee of Shenzhen Institutes of Advanced Technology and all the animal experiments were carried out ethically and humanely. To obtain the breast tumor model, about 1×10^6 MCF-7 cells were injected orthotopically into the mammary fat pad of each mouse. The treatment started when the tumor volume reached approximately 150–200 mm^3.

2.9.1. Fluorescence labeling of Bi_2Se_3-laden-macrophages for in vivo imaging

To obtain the Bi_2Se_3-laden-macrophages, 1×10^5 RAW264.7 cells were cultured for 12 h and co-incubated with 20 ppm Bi_2Se_3 nanosheets for an additional 24 h. Afterwards, the Bi_2Se_3-laden-macrophages were labeled by the NIR fluorescent dye DIR, rinsed, redispersed in PBS, and intravenously injected into the tumor-bearing BALB/c nude mice. At 24 h post-injection of Bi_2Se_3-laden-macrophages, the tumor-bearing mice were sacrificed. The major organs were excised and imaged to obtain the tissue distribution of the DIR labeled Bi_2Se_3-laden-macrophages on an *ex/in vivo* fluorescence imaging system (Maestro). The Bi and Se concentrations were determined by ICP-OES. The bare DIR labeled macrophages were used as the control.

2.9.2. In vivo photothermal cancer therapy

The BALB/c nude mice bearing MCF-7 tumors were randomly divided into three groups (n = 20 for each group) and each group was intravenously injected with 150 μL of PBS (control), bare Bi_2Se_3 nansheets (20 μg/g), or Bi_2Se_3-laden-macrophages (~20 μg Bi_2Se_3 nansheets in 1.5×10^6 RAW264.7 cells/g) *via* the tail vein. After 24 h, the mice bearing tumors were anesthetized and the entire tumors were exposed to the laser (808 nm, 1.0 W/cm^2) for 10 min. During laser irradiation, an infrared thermal imaging camera was utilized to monitor the temperature changes in the tumor sites. The changes in the tumor volume post-irradiation were measured by a caliper every day and the tumor volume V (mm^3) was calculated according to the formula: Volume = (Tumor length) × (Tumor width)^2/2. The relative tumor volumes were calculated as V/V_o, where V_o was the tumor volume at the beginning of PTT.

2.9.3. Blood analysis and tissue analysis

In the blood analysis, healthy BALB/c mice were injected intravenously with the bare Bi_2Se_3 nansheets (dose = 20 μg/g) or Bi_2Se_3-laden-macrophages (~20 μg Bi_2Se_3 nansheets in 1.5 × 10^6 RAW264.7 cells/g), and blood was collected for chemical tests at 10 and 20 days post-injection. In the tissue analysis, the healthy BALB/c mice were injected intravenously with the bare Bi_2Se_3 nansheets (dose = 20 μg/g) or Bi_2Se_3-laden-macrophages (~20 μg Bi_2Se_3 nansheets in 1.5 × 10^6 RAW264.7 cells/g) for 20 days and the major organs were collected, fixed in 4% formalin, sectioned to a thickness of 5 μm, and stained with haematoxylin and eosin for microscopic examination.

2.9.4. Biodistribution and clearance

The BALB/c mice were randomly divided into two groups (n = 6 for each group) and injected intravenously with Bi_2Se_3 nansheets (dose = 20 μg/g) or Bi_2Se_3-laden-macrophages (~20 μg Bi_2Se_3 nansheets in 1.5 × 10^6 RAW264.7 cells/g) *via* the tail vein. To determine the Bi_2Se_3 biodistribution *in vivo*, the injected mice ($n = 25$ per group) were euthanized at different time intervals and the major organs and blood were collected, wet-weighed, and digested in 5 mL of HNO_3. Finally, the Bi and Se concentrations were determined by ICP-OES. To evaluate Bi_2Se_3 elimination *in vivo*, the injected mice were euthanized at 1, 5, 10, 15, 20 and 25 days. The major organs were excised, wet-weighed, and digested and the contents of Bi and Se were determined by ICP-OES as described above.

2.10. Statistical analysis

The experimental results were expressed as means ± standard deviations (SD). The significance of difference was analyzed by one-way analysis of variance followed by the Tukey's honestly significant difference (HSD) test using SPSS 13.0 (SPSS Inc.). A value of $p < 0.05$ was considered to be significant.

3. Results and discussion

3.1. Characterization of Bi_2Se_3 nanosheets

The Bi_2Se_3 nanosheets are characterized by TEM and Fig. 2(a) and (b) reveal that the products have a relatively uniform size distribution and are mainly bilayered nanosheets with a second triangular layer stacking on the primary one. According to the statistical TEM analysis of 200 particles, the average size of the Bi_2Se_3 nanosheets is 84.0 ± 11.3 nm. The HR-TEM image in Fig. 2(c) shows a hexagonal lattice with a spacing of 0.21 nm corresponding to the (110) plane of the Bi_2Se_3 crystal [59,60]. Fig. 2(d) shows the AFM image of the Bi_2Se_3 nanosheets and the insets depict the topographical image of a single nanosheet and corresponding sectional analysis. The Bi_2Se_3 nanosheets have a layered structure and the thicknesses of the first layer and triangular second layer are both about 4 nm corresponding to a stack of 4 quintuple layers [61]. As shown in the XRD patterns in Fig. 2(e), all the peaks can be indexed to the rhombohedral phase of Bi_2Se_3 consistent with the peaks of bulk Bi_2Se_3 (JCPDS Card No. 33-0214) [62]. EDS [Fig. 2(f)] and ICP-OES [Table S1] disclose uniform distribution of Bi and Se with an atomic ratio of 2:3.

The optical absorption spectra of the Bi_2Se_3 nanosheets are acquired on a UV-visible-NIR spectrophotometer. As shown in Fig. 2(g), the absorption spectra of Bi_2Se_3 nanosheets span the UV and NIR regions similar to other 2D materials such as GO [13] and

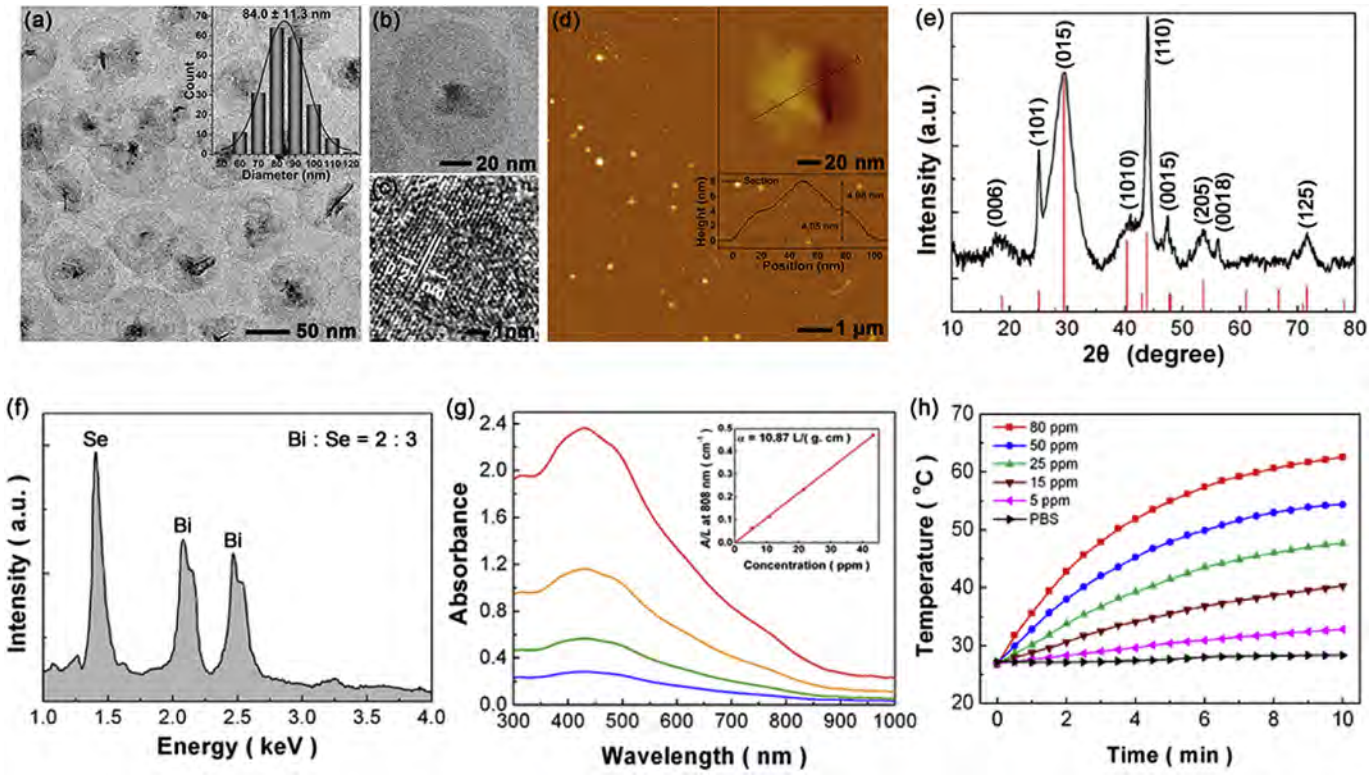

Fig. 2. Characterization of Bi_2Se_3 nanosheets: (a) TEM image and inset showing the statistical size analysis of 200 particles measured by TEM; (b) Magnified TEM image; (c) HR-TEM image; (d) AFM images; (e) XRD spectra; (f) EDS spectra; (g) Absorbance spectra of the Bi_2Se_3 nanosheets dispersed in water at concentrations of 5.4, 10.8, 21.6, 43.2 ppm. Inset: absorbance intensity normalized over the characteristic length of cell (A/L) for $\lambda = 808$ nm at different concentrations; (h) Photothermal heating curves of different concentrations of Bi_2Se_3 nanosheets under NIR irradiation (808 nm, 1.0 W/cm^2).

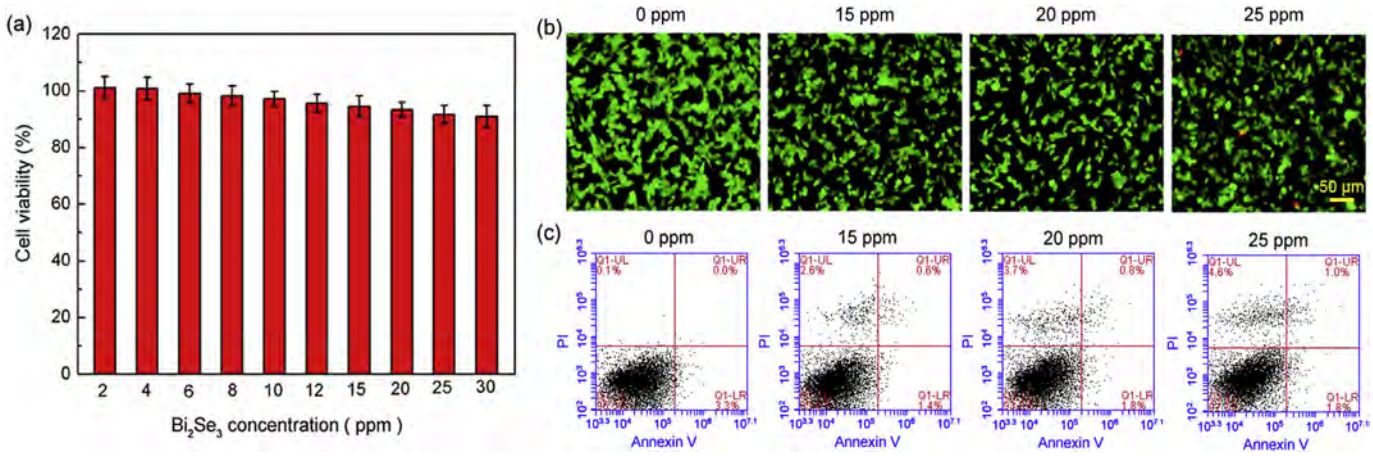

Fig. 3. Cytocompatibility of Bi_2Se_3 nanosheets to RAW26.7 macrophages: (a) MTT assay; (b) Calcein AM/PI staining (viable cells are stained green with Calcein AM and dead cells are stained red with PI); (c) Flow cytometric analysis. (For interpretation of the references to colour in this figure legend, the reader is referred to the web version of this article.)

WS_2 [22]. The absorption intensity at 808 nm is normalized over the characteristic length of cell (A/L) and determined at different concentrations (C). In agreement with the Lambert-Beer law ($A/L = \alpha C$, where α is the extinction coefficient), a linear trend is observed from A/L versus concentration when the extinction coefficient at 808 nm is 10.9 L g^{-1} cm^{-1}. It is about 2.8 times of the 808 nm extinction coefficient (3.9 L g^{-1} cm^{-1}, see Fig. S1) of Au nanorods (one of the extensively studied photothermal agents) [29].

The NIR photothermal performance of the Bi_2Se_3 nanosheets (5, 15, 25, 50, and 80 ppm) is studied and the results are presented in Fig. 2(h). In contrast to the control PBS solution, the Bi_2Se_3 nanosheets suspension exhibits excellent photothermal heating under NIR light irradiation. In particular, at a concentration of 50 ppm, the temperature of the Bi_2Se_3 nanosheets rises from 27.0 °C to 54.4 °C after NIR irradiation for 10 min and the temperature is high enough for photothermal ablation of cancer cells. In the meantime, the temperature of the PBS solution increases only slightly from 27.2 °C to 28.3 °C. According to the previously reported method [7], the photothermal conversion efficiency of Bi_2Se_3 nanosheets is calculated to be 26.4% (Fig. S2), which is higher than that of gold nanorods (21.0%). The high photothermal conversion efficiency of 2D Bi_2Se_3 bodes well for photothermal therapy.

3.2. Cytocompatibility investigation

The methyl thiazolyltetrazolium (MTT) assay is employed to evaluate the cytocompatibility of Bi_2Se_3 nanosheets when the viability of untreated cells is assumed to be 100%. As shown in Fig. 3(a), the cell viability is nearly 95% or above when the concentration of Bi_2Se_3 nanosheets is below 10 ppm. Even when the concentration of Bi_2Se_3 nanosheets is increased to 100 ppm (5 times larger than the Bi_2Se_3-laden-macrophages uptake dose in this study), the cell viability remains at 85.40 ± 3.27% (Fig S3). The good biocompatibility of Bi_2Se_3 nanosheets is probably because Bi is an environmentally friendly element and Se is an essential trace element [34].

The cytocompatibility of the Bi_2Se_3 nanosheets is evaluated by calcein AM/PI live/dead cell staining (viable cells are stained green with Calcein AM and dead ones are stained red with PI) and flow cytometry. The fluorescence images in Fig. 3(b) indicate that almost no dead cell with red fluorescence can be found even when the macrophages are co-incubated with 25 ppm of Bi_2Se_3 nanosheets. Fig. 3(c) reveals the flow cytometry graphs of RAW264.7 cells after co-incubation with Bi_2Se_3 nanosheets with different concentrations (15, 20, 25 ppm). It is evident that the cells suffer low-level apoptosis and necrosis (cells mortality is below 7.3%) at a high concentration of Bi_2Se_3 nanosheets of 25 ppm. Evidently, the Bi_2Se_3 nanosheets are desirable in macrophages delivery and their low cytotoxicity is confirmed with MCF-7 cells (Figs. S4 and S5).

3.3. Macrophages uptake of Bi_2Se_3 nanosheets

Sufficient cellular uptake of Bi_2Se_3 nanosheets by macrophages is prerequisite to cellular delivery as photothermal agents. As shown in the bright-field images in Fig. 4(a), the macrophages can uptake Bi_2Se_3 nanosheets efficiently after exposure to the Bi_2Se_3 nanosheets for 24 h. The cells engulfing Bi_2Se_3 are partially opaque

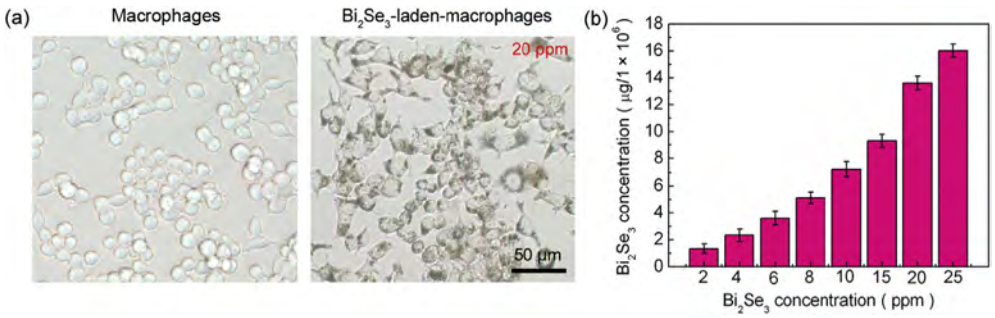

Fig. 4. Macrophages uptake of Bi_2Se_3 nanosheets: (a) Bright-field images of macrophages before and after uptake of Bi_2Se_3 nanosheets; (b) Quantitative determination of macrophages uptake of Bi_2Se_3 nanosheets.

in the cytoplasm due to the original color of Bi_2Se_3 nanosheets [26] suggesting a high uptake efficiency.

The uptake efficiency of Bi_2Se_3 nanosheets is further investigated by ICP-OES and as shown in Fig. 4(b), the macrophages uptake of Bi_2Se_3 nanosheets shows a typical dose-dependent manner. When the concentration of the Bi_2Se_3 nanosheets is 20 ppm, the cellular uptake Bi_2Se_3 nanosheets increases to 13.62 ± 0.50 μg/1×10^6 macrophages. It is worth noting that when the Bi_2Se_3 nanosheets concentration reaches 25 ppm, the cellular uptake can be as high as 16.03 ± 0.49 μg/1×10^6 macrophages. On account of the low cytotoxicity and high uptake efficiency, a dose of 20 ppm Bi_2Se_3 nanosheets has advantages in macrophages loading and in subsequent studies, macrophages laden with 20 ppm of Bi_2Se_3 nanosheets (named Bi_2Se_3-laden-macrophages) are chosen as the typical model to access the performance *in vivo*.

3.4. *In vivo* biodistribution and tumor targeting of Bi_2Se_3-laden-macrophages

To investigate the feasibility of macrophages targeted delivery of Bi_2Se_3 nanosheets to the tumor region, bare macrophages and Bi_2Se_3-laden-macrophages are labeled with a NIR dye DIR (KGMP0026) and intravenously injected into the BALB/c nude mice bearing MCF-7 tumor. DIR fluorescence images are obtained after different time frames [63] and as shown in Fig. 5(a), the bare macrophages and Bi_2Se_3-laden-macrophages are very similar in the tracking trend. The macrophages are distributed rapidly in the liver due to reticuloendothelial systems (RES) absorption. At 3 h after intravenous injection, the macrophages invade the spleen and after 6 h, the tumor tracking trend can be observed. The fluorescence intensity in the tumor site gradually increases up to 24 h, and the tumor retains strong fluorescence at 48 h after intravenous injection. Fig. 5(b–d) depict the *ex vivo* fluorescence images 24 h after intravenous injection. The tumor and some organs such as liver, spleen, and lung are bright in fluorescence. The transverse section images (Fig. 5(e)) further reveal that most of the macrophages can deliver the Bi_2Se_3 to the entire tumors after overcoming the hypoxia-associated drug delivery barrier.

The Bi and Se elemental biodistribution of Bi_2Se_3-laden-macrophages in the mice is quantitatively determined by ICP-OES with the bare Bi_2Se_3 nanosheets as the control [see Fig. 5(f and g)]. After direct intravenous injection of Bi_2Se_3 nanosheets without macrophages delivery, a large concentration of Bi and Se accumulates in the liver and spleen, while it is relatively small at the tumor. It is possibly because tumor uptake of Bi_2Se_3 nanosheets depends on the passive EPR effect and it is difficult to overcome the hypoxia-associated drug delivery barrier [57,64]. On the contrary, the Bi_2Se_3-laden-macrophages possess a much higher tumor-targeting efficiency with Bi concentration of 39.54 ± 6.84 μg/g and Se of 11.21 ± 2.71 μg/g, which are 3–4 times larger than those of the Bi_2Se_3 group. The Bi_2Se_3-laden-macrophages also can efficiently reduce Bi_2Se_3 nanosheets accumulation in the reticuloendothelial (liver, spleen) and urinary (kidney) systems.

3.5. *In vivo* photothermal cancer therapy

In vivo experiments are performed to evaluate the capability of Bi_2Se_3-laden-macrophages in photothermal cancer therapy. In particular, 60 BALB/c nude mice bearing MCF-7 breast tumors are randomly divided into three groups after the tumor volume reaches approximately 200 mm^3. The PBS solution (150 μL), bare Bi_2Se_3 nanosheets (~20 μg/g), and Bi_2Se_3-laden-macrophages (~20 μg Bi_2Se_3 nanosheets in 1.5×10^6 RAW264.7 cells/g) are separately and intravenously injected into the experimental mice *via* the tail vein. At 24 h after intravenous injection, the mice are anesthetized and the region of tumor site is NIR irradiated (808 nm, 1.0 W/cm^2) for up to 10 min. In the meantime, an infrared thermal imaging camera is utilized to monitor the photothermal effects *in vivo* by mapping the temperature change of tumor sites.

As shown in Fig. 6(a) and (b), owing to the photothermal effect of Bi_2Se_3 nanosheets, the tumor temperature increase of the bare Bi_2Se_3 group is about 20.6 °C under NIR irradiation, which is much larger than that of the PBS group (9.0 °C). In the Bi_2Se_3-laden-macrophages group, the tumor temperature rapidly increases by 32.2 °C within only 3 min of NIR irradiation by reaching a temperature of almost 60.1 °C for tumor ablation. These results indicate the high efficiency of Bi_2Se_3-laden-macrophages with respect to *in vivo* photothermal tumor ablation because the cell delivery improves tumor targeting and coverage of the Bi_2Se_3 nanosheets. The histological examination of tumor slices in Fig. 6(c) reveals that a large amount of tumor cells are severely destroyed by PTT with Bi_2Se_3-laden-macrophages, suggesting that tumor ablation is effective. In comparison, the tumors treated with Bi_2Se_3 nanosheets are only partially damaged and no obvious damage in the tumor cells can be found from the PBS group.

After the photothermal treatment, all the experimental mice are measured for the tumor size every day, and no obvious side effects such as abnormal body weight (see Fig. S6) can be observed. As shown in Fig. 6(d)–(f), no tumor inhibition is found from the control group treated with PBS and all the mice died within 22 days post-irradiation. On the other hand, the Bi_2Se_3-laden-macrophages group shows complete tumor ablation and all the mice are alive until the end of the experiment (45 days post-irradiation) without tumor recurrence. With regard to the bare Bi_2Se_3 group, although tumor growth is partially inhibited by the PTT effect of Bi_2Se_3 in the first 4 days, rapid tumor recovery and growth are observed thereafter and all the mice die within 32 days. The results demonstrate that the Bi_2Se_3-laden-macrophages are efficient PTT agents in photothermal ablation of tumors.

3.6. *In vivo* toxicity

The potential toxicity of Bi_2Se_3-laden-macrophages is evaluated by blood biochemical and histology analysis *in vivo*. In the blood analysis, healthy BALB/c mice are injected intravenously with PBS, Bi_2Se_3 nansheets (~20 μg/g) or Bi_2Se_3-laden-macrophages (~20 μg Bi_2Se_3 nansheets in 1.5×10^6 RAW264.7 cells/g), and blood is collected after 10 and 20 days. Various parameters including the total proteins, alkaline phosphatase (ALP), serum albumin (ALB), alanine aminotransferase (ALT), aspartate aminotransferase (AST), globulin (GOLB), kidney function marker urea nitrogen (BUN), creatinine (CREA), albumin/globin (A/G) are examined [Fig. 7(a)] [58,65]. Compared to the PBS group, no significant difference can be detected from the Bi_2Se_3 group and Bi_2Se_3-laden-macrophages group at all time points, indicating very little influence on the blood chemistry of mice. In the histology analysis, the mice are euthanized after 20 days and the major organs including the heart, liver, spleen, lung, and kidney are collected and sliced for H&E staining [66]. Evidently, no organ damage or inflammatory lesion can be observed from the control and experimental groups during the treatment period corroborating the good *in vivo* biocompatibility of the Bi_2Se_3-laden-macrophages.

3.7. *In vivo* biodistribution and clearance

The ideal biomaterials should have a long circulation time in blood and rapid clearance from major organs afterwards. In this respect, the pharmacokinetics profiles of Bi_2Se_3 nanosheets and Bi_2Se_3-laden-macrophages are examined by ICP-OES. As shown in Fig. 8(a) and (b), blood circulation obeys a biexponential

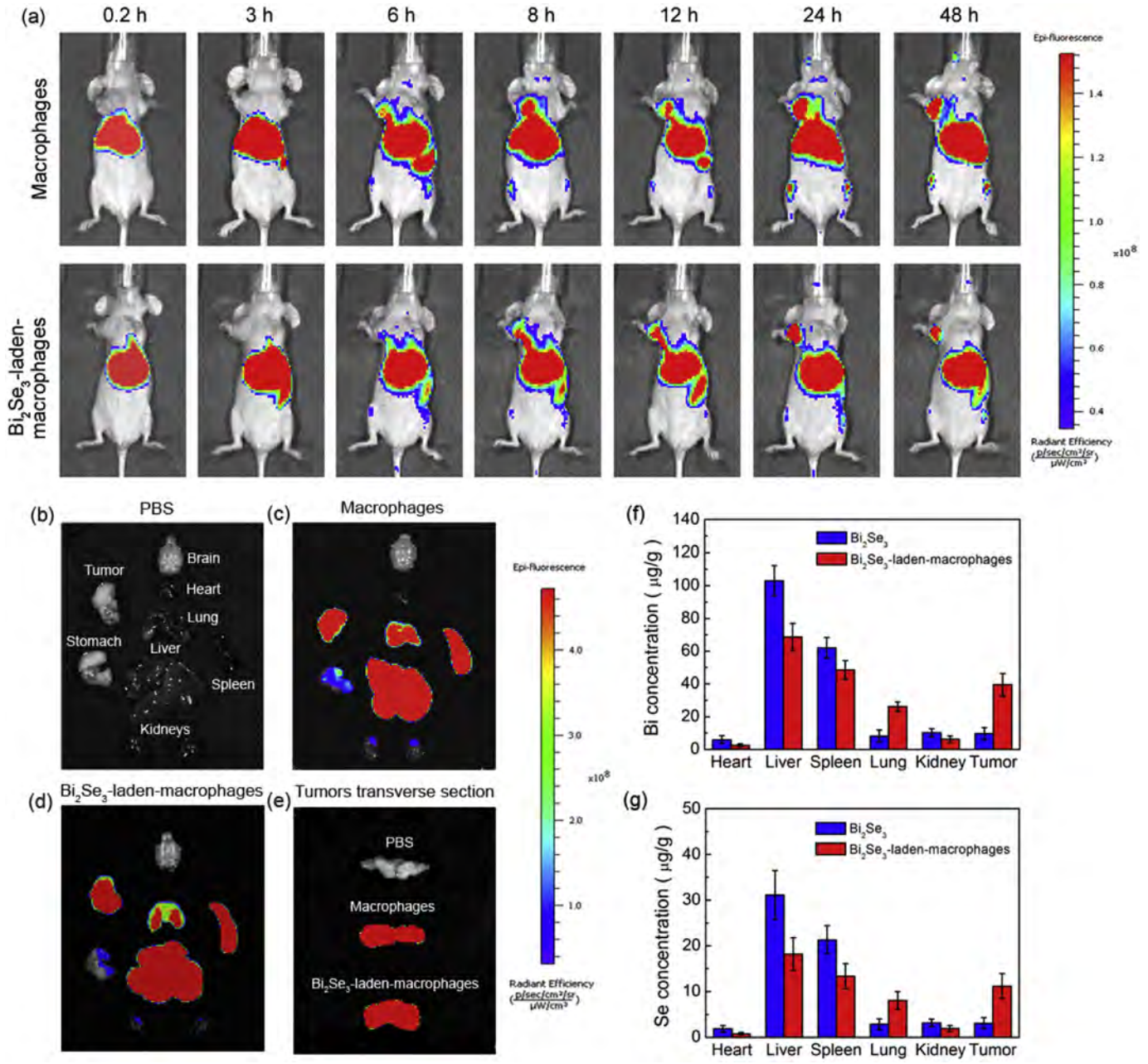

Fig. 5. *In vivo* biodistribution of macrophages and Bi_2Se_3-laden-macrophages in mice bearing MCF-7 tumors: (a) *In vivo* fluorescence tracking of the dye-labeled macrophages and dye-labeled Bi_2Se_3-laden-macrophages after intravenous injection; (b–d) *Ex vivo* fluorescence images of the tumors and major organs at 24 h after intravenous injection of (b) PBS, (c) dye-labeled macrophages, and (d) dye-labeled Bi_2Se_3-laden-macrophages; (e) Fluorescence images of the tumor transverse section of mice injected with PBS, dye-labeled macrophages and dye-labeled Bi_2Se_3-laden-macrophages; (f, g) Biodistribution of (f) Bi and (g) Se at 24 h post-injection of the bare Bi_2Se_3 nanosheets and Bi_2Se_3-laden-macrophages.

relationship. Based on the blood circulation curves in Fig. 8(a) and (b), the pharmacokinetics data can be estimated by using a two-compartment model and the corresponding results are summarized in Table S2. In particular, the Bi $t_{1/2}\alpha$ (blood distribution half-life) and $t_{1/2}\beta$ (blood terminal elimination half-life) of the Bi_2Se_3-laden-macrophages group are 0.84 ± 0.01 h and 15.58 ± 1.90 h, respectively. The Se $t_{1/2}\alpha$ is 0.72 ± 0.03 h and $t_{1/2}\beta$ is 8.50 ± 1.56 h, which are much longer than those of the Bi_2Se_3 nanosheets group (Bi $t_{1/2}\alpha$ = 0.34 ± 0.02 h, Se $t_{1/2}\alpha$ = 0.56 ± 0.02 h, Bi $t_{1/2}\beta$ = 6.42 ± 1.50 h, Se $t_{1/2}\beta$ = 7.28 ± 2.99 h). Moreover, in the Bi_2Se_3-laden-macrophages group, the corresponding $AUC_{0\text{-}25\ days}$ (area under the concentration-time curve from 0 to 25 days) of Bi is 669.00 ± 93.01 μg/mL*h and Se is 258.32 ± 52.81 μg/mL*h, which are significantly higher than that of the Bi_2Se_3 nanosheets ($AUC_{0\text{-}25\ days}$ of Bi = 331.41 ± 77.33 μg/mL*h, $AUC_{0\text{-}25\ days}$ of Se = 95.11 ± 44.58 μg/mL*h), suggesting higher bioavailability and lower clearance of the Bi_2Se_3-laden-macrophages (Table S2). Macrophages delivery can significantly prolong blood circulation of the Bi_2Se_3 nanosheets enabling efficient tumor accumulation and avoiding rapid particle clearance from the circulating blood into RES systems [67,68].

To investigate the long-term biodistribution and clearance of the materials, 150 μL of the Bi_2Se_3 nanosheets (~20 μg/g) and Bi_2Se_3-laden-macrophages (~20 μg Bi_2Se_3 nansheets in 1.5 × 10^6

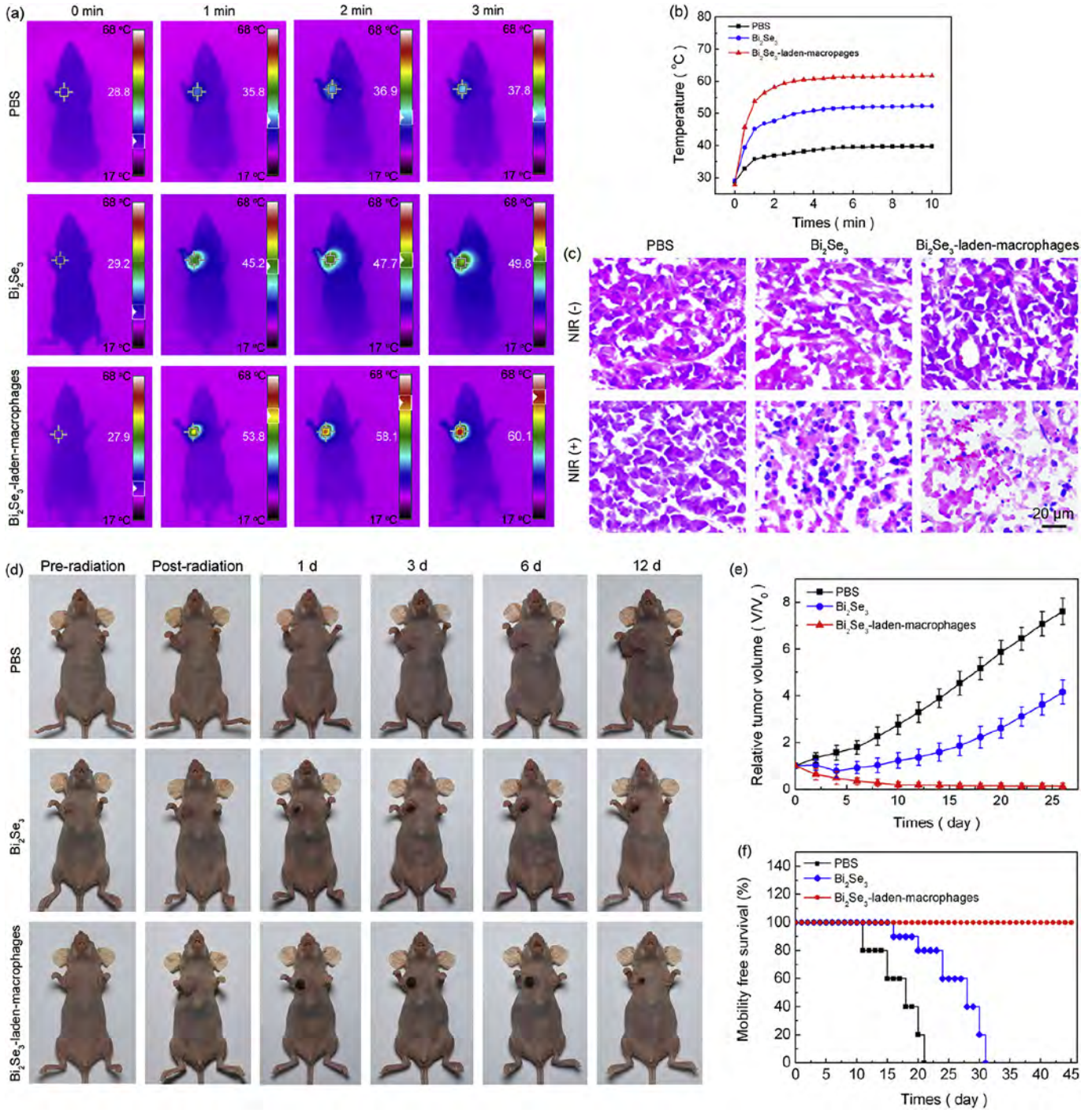

Fig. 6. *In vivo* photothermal cancer therapy of BALB/c nude mice bearing MCF-7 breast tumors under 10 min of NIR irradiation (808 nm, 1.0 W/cm^2) at 24 h post-injection of PBS, Bi_2Se_3 nanosheets, and Bi_2Se_3-laden-macrophages intravenously: (a) IR thermal images of the mice; (b) Curves of tumor temperature versus time; (c) H&E staining of tumor sections; (d) Typical mice before and after PTT treatments for 0, 1, 3, 6, and 12 days; (e) Tumor growth curves of different groups of mice; (f) Survival curves of different groups of mice.

RAW264.7 cells/g) are injected into the healthy BALB/c mice (50 mice, 25 mice per group) intravenously. The mice are sacrificed at 1, 5, 10, 15, and 30 days after intravenous injection and the main organs including liver, spleen, kidney, lung, and heart are separated and analyzed by ICP-OES to determine the distributions of Bi and Se contents [see Fig. 8(c–e)]. In both groups, the liver and spleen show dominant accumulation of Bi and Se which is probably due to RES absorption. Notably, the Bi and Se concentrations in the major organs diminish gradually with time. Fig. 8(c) and (d) show that the Bi and Se residual ratios (residual amount/initial amount) of the Bi_2Se_3-laden-macrophages group are smaller than those of the Bi_2Se_3 nanosheets group. At the first day post-injection, the Bi and Se residual ratios of the Bi_2Se_3-laden-macrophages group is 58.01 ± 7.71% and 42.96 ± 4.63%, respectively, whereas those of the Bi_2Se_3 nanosheets group are 83.45 ± 9.07% and 58.39 ± 6.81%, confirming that macrophages delivery can efficiently reduce rapid

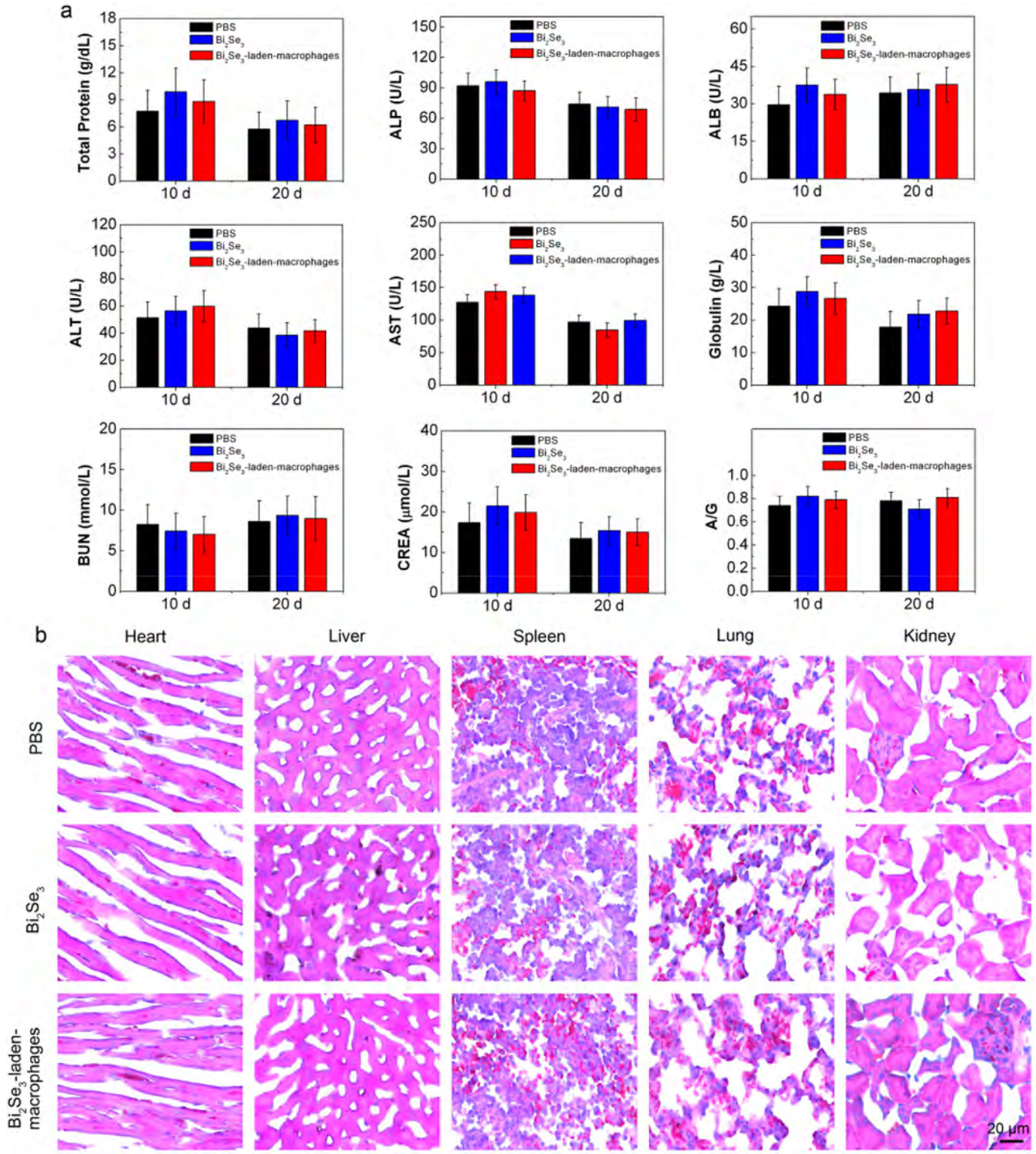

Fig. 7. *In vivo* toxicity assay of the Bi_2Se_3 nanosheets and Bi_2Se_3-laden-macrophages with PBS as the control: (a) Blood biochemistry analysis of different groups of mice at 10 and 20 days post-injection; (b) Histological observation of the major organs of different groups of mice at 20 days post-injection.

particle clearance by the RES systems. At the 25th day, the Bi residual ratio of the Bi_2Se_3-laden-macrophages group decreases to 3.74 ± 1.71% and Se residual ratio is 3.63 ± 1.61%, whereas for the Bi_2Se_3 nanosheets group, Bi is 12.17 ± 2.66% and Se is 6.24 ± 2.22%. Macrophages-mediated delivery leads to more efficient clearance of the Bi_2Se_3 nanosheets from the body and it is probably because the RES systems with a lighter burden enables proper clearance functions. The efficient *in vivo* clearance capability minimizes the risk of long-term accumulation of the Bi_2Se_3 nanosheets.

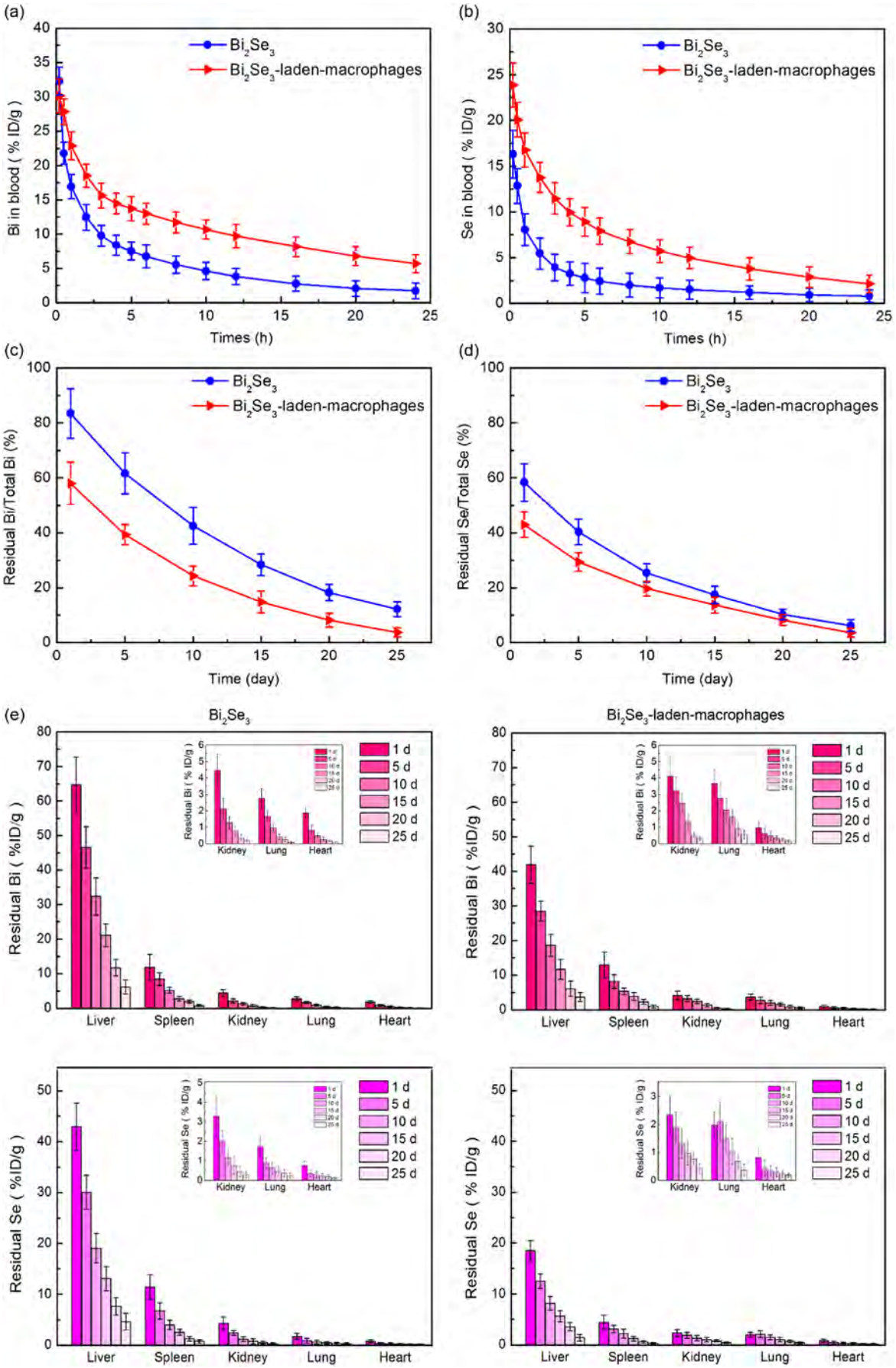

Fig. 8. Biodistribution and clearance of Bi_2Se_3 nanosheets and Bi_2Se_3-laden-macrophages *in vivo* after intravenous injection: (a, b) Blood circulation curves of (a) Bi and (b) Se at different time points post-injection; (c, d) Residual ratios versus time post-injection of (c) Bi and (d) Se; (e) Residual Bi (up) and Se (down) biodistributions in different organs at different time points post-injection.

4. Conclusion

Bi_2Se_3-laden-macrophages constitute an efficient delivery system in photothermal cancer therapy. The strategy utilizes macrophages as "Trojan horses" carrying 2D Bi_2Se_3 nanosheets with high NIR photothermal performance, high macrophage uptake, and negligible cytotoxicity. Possessing prolonged blood circulation and minimized rapid RES absorption, the Bi_2Se_3-laden-macrophages after intravenous injection have higher tumor targeting efficiency than bare Bi_2Se_3 by overcoming the hypoxia-associated drug delivery barrier consequently giving rise to high-efficient tumor ablation capability under NIR irradiation. The Bi_2Se_3-laden-macrophages exhibit no appreciable toxicity and good biocompatibility as shown by blood biochemical and histological analyses and most of the materials can be efficiently excreted from the body within 25 days. These results demonstrate that the Bi_2Se_3-laden-macrophages constitute a highly efficient PTT system by optimizing the *in vivo* agent delivery and photothermal efficiency and this cell-mediated strategy can be further extended to other nanomaterials or drug-based therapies.

Acknowledgments

We gratefully acknowledge the financial support by the National Natural Science Foundation of China (51672305, 81501592), Science and Technology Basic Projects of Shenzhen (JCYJ20150401145529032, JCYJ20120615124830232), China Postdoctoral Science Foundation funded project (2016T90807, 2015M582445), Guangdong Natural Science Foundation Doctoral project (2015A030310210), Hong Kong Scholars Program (XJ2016044), Hong Kong Research Grants Council (RGC) General Research Funds (GRF) CityU No. 11301215, and City University of Hong Kong Strategic Research Grant (SRG) No. 7004644.

Appendix A. Supplementary data

Supplementary data related to this article can be found at http://dx.doi.org/10.1016/j.biomaterials.2017.04.012.

References

[1] D. Ho, C.H. Wang, E.K. Chow, Nanodiamonds: the intersection of nanotechnology, drug development, and personalized medicine, Sci. Adv. 1 (2015) e1500439.
[2] G.Y. Chen, I. Roy, C.H. Yang, P.N. Prasad, Nanochemistry and nanomedicine for nanoparticle-based diagnostics and therapy, Chem. Rev. 116 (2016) 2826–2885.
[3] C.A. Aaron, M. Samir, Nanoparticles in the clinic, Bioeng. Transl. Med. 1 (2016) 10–29.
[4] J.A. Barreto, W. O'Malley, M. Kubeil, B. Graham, H. Stephan, L. Spiccia, Nanomaterials: applications in cancer imaging and therapy, Adv. Mater. 23 (2011) 18–40.
[5] L.R. Hirsch, R.J. Stafford, J.A. Bankson, J.A. Bankson, S.R. Sershen, B. Rivera, et al., Nanoshell-mediated near-infrared thermal therapy of tumors under magnetic resonance guidance, Proc. Natl. Acad. Sci. U. S. A. 11 (2003) 13549–13554.
[6] L. Cheng, C. Wang, L.Z. Feng, K. Yang, Z. Liu, Functional nanomaterials for phototherapies of cancer, Chem. Rev. 114 (2014) 10869–10939.
[7] C.M. Hessel, V.P. Pattani, M. Rasch, M.G. Panthani, B. Koo, J.W. Tunnell, et al., Copper selenide nanocrystals for photothermal therapy, Nano Lett. 11 (2011) 2560–2566.
[8] J. Mou, P. Li, C.B. Liu, H.X. Xu, L. Song, J. Wang, et al., Ultrasmall $Cu_{2-x}S$ nanodots for highly efficient photoacoustic imaging-guided photothermal therapy, Small 11 (2015) 2275–2283.
[9] C.X. Guo, Y.S. Jin, Z.F. Dai, Multifunctional ultrasound contrast agents for imaging guided photothermal therapy, Bioconjugate Chem. 25 (2014) 840–854.
[10] R. Kurapati, K. Kostarelos, M. Prato, A. Bianco, Biomedical uses for 2D materials beyond graphene: current advances and challenges ahead, Adv. Mater. 28 (2016) 6052–6074.
[11] H. Zhang, Ultrathin two-dimensional nanomaterials, ACS Nano 9 (2015) 9451–9469.
[12] B. Tian, C. Wang, S. Zhang, L. Feng, Z. Liu, Photothermally enhanced photodynamic therapy delivered by nano-graphene oxide, ACS Nano 5 (2011) 7000–7009.
[13] J.T. Robinson, S.M. Tabakman, Y. Liang, H. Wang, H.S. Casalongue, D. Vinh, et al., Ultrasmall reduced graphene oxide with high near-infrared absorbance for photothermal therapy, J. Am. Chem. Soc. 133 (2011) 6825–6831.
[14] K. Yang, J. Wan, S. Zhang, B. Tian, Y. Zhang, Z. Liu, The influence of surface chemistry and size of nanoscale graphene oxide on photothermal therapy of cancer using ultra-low laser power, Biomaterials 33 (2012) 2206–2214.
[15] K. Yang, S. Zhang, G. Zhang, X. Sun, S.T. Lee, Z. Liu, Graphene in mice: ultrahigh *in vivo* tumor uptake and efficient photothermal therapy, Nano Lett. 10 (2010) 3318–3323.
[16] D.Z. Yang, L.Z. Feng, C.A. Dougherty, K.E. Luker, D.Q. Chen, M.A. Cauble, et al., *In vivo* targeting of metastatic breast cancer *via* tumor vasculature-specific nano-graphene oxide, Biomaterials 104 (2016) 361–371.
[17] S.S. Chou, B. Kaehr, J. Kim, B.M. Foley, M. De, P.E. Hopkins, et al., Chemically exfoliated MoS_2 as near-infrared photothermal agents, Angew. Chem. Int. Ed. Engl. 52 (2013) 4160–4164.
[18] W. Feng, L. Chen, M. Qin, X. Zhou, Q. Zhang, Y. Miao, et al., Flower-like PEGylated MoS_2 nanoflakes for near-infrared photothermal cancer therapy, Sci. Rep. 5 (2015) 17422.
[19] Y. Chen, C. Tan, H. Zhang, L. Wang, Two-dimensional graphene analogues for biomedical applications, Chem. Soc. Rev. 44 (2015) 2681–2701.
[20] T. Liu, S. Shi, C. Liang, S. Shen, L. Cheng, C. Wang, et al., Iron oxide decorated MoS_2 nanosheets with double PEGylation for chelator-free radiolabeling and multimodal imaging guided photothermal therapy, ACS Nano 9 (2015) 950–960.
[21] Z.Y. Lei, W.C. Zhu, S.J. Xu, J. Ding, J.X. Wan, P.Y. Wu, Hydrophilic $MoSe_2$ nanosheets as effective photothermal therapy (PTT) agent and their applications in smart devices, ACS Appl. Mater. Interfaces 8 (2016) 20900–20908.
[22] L. Cheng, J. Liu, X. Gu, H. Gong, X. Shi, T. Liu, et al., PEGylated WS_2 nanosheets as a multifunctional theranostic agent for *in vivo* dual-modal CT/photoacoustic imaging guided photothermal therapy, Adv. Mater. 26 (2014) 1886–1893.
[23] X.R. Song, X.Y. Wang, S.X. Yu, J.B. Cao, S.H. Li, J. Li, et al., Co_9Se_8 nanoplates as a new theranostic platform for photoacoustic/magnetic resonance dual-modal-imaging-guided chemo-photothermal combination therapy, Adv. Mater. 27 (2015) 3285–3291.
[24] L. Cheng, C. Yuan, S. Shen, X. Yi, H. Gong, K. Yang, et al., Bottom-up synthesis of metal-ion-doped WS_2 nanoflakes for cancer theranostics, ACS Nano 9 (2015) 11090–11101.
[25] J. Liu, X. Zheng, L. Yan, L. Zhou, G. Tian, W. Yin, et al., Bismuth sulfide nanorods as a precision nanomedicine for *in vivo* multimodal imaging-guided photothermal therapy of tumor, ACS Nano 9 (2015) 696–707.
[26] H.H. Xie, Z.B. Li, Z.B. Sun, J.D. Shao, X.F. Yu, Z.N. Guo, et al., Metabolizable ultrathin Bi_2Se_3 nanosheets in imaging-guided photothermal therapy, Small 12 (2016) 4136–4145.
[27] V. Eswaraiah, Q. Zeng, Y. Long, Z. Liu, Black phosphorus nanosheets: synthesis, characterization and applications, Small 12 (2016) 3480–3502.
[28] C.X. Sun, L. Wen, J.F. Zeng, Y. Wang, Q. Sun, L.J. Deng, et al., One-pot solventless preparation of PEGylated black phosphorus nanoparticles for photoacoustic imaging and photothermal therapy of cancer, Biomaterials 91 (2016) 81–89.
[29] Z.B. Sun, H.H. Xie, S.Y. Tang, X.F. Yu, Z.N. Guo, J.D. Shao, et al., Ultrasmall black phosphorus quantum dots: synthesis and use as photothermal agents, Angew. Chem. Int. Ed. Engl. 54 (2015) 11526–11530.
[30] D. Chimene, D.L. Alge, A.K. Gaharwar, Two-dimensional nanomaterials for biomedical applications: emerging trends and future prospects, Adv. Mater. 27 (2015) 7261–7284.
[31] T. Liu, C. Wang, X. Gu, H. Gong, L. Cheng, X. Shi, et al., Drug delivery with PEGylated MoS_2 nano-sheets for combined photothermal and chemotherapy of cancer, Adv. Mater. 26 (2014) 3433–3440.
[32] G.B. Yang, H. Gong, T. Liu, X.Q. Sun, L. Cheng, Z. Liu, Two-dimensional magnetic WS_2@Fe_3O_4 nanocomposite with mesoporous silica coating for drug delivery and imaging-guided therapy of cancer, Biomaterials 60 (2015) 62–71.
[33] W. Yin, L. Yan, J. Yu, G. Tian, L. Zhou, X. Zheng, et al., High-throughput synthesis of single-Layer MoS_2 nanosheets as a near-infrared photothermal-triggered drug delivery for effective cancer therapy, ACS Nano 8 (2014) 6922–6933.
[34] J. Li, F. Jiang, B. Yang, X.R. Song, Y. Liu, H.H. Yang, et al., Topological insulator bismuth selenide as a theranostic platform for simultaneous cancer imaging and therapy, Sci. Rep. 3 (2013) 1998.
[35] L. Rao, L.L. Bu, B. Cai, J.H. Xu, A. Li, W.F. Zhang, et al., Cancer cell membrane-coated upconversion nanoprobes for highly specific tumor imaging, Adv. Mater. 28 (2016) 3460–3466.
[36] S. Wilhelm, A.J. Tavares, Q. Dai, S. Ohta, J. Audet, H.F. Dvorak, et al., Analysis of nanoparticle delivery to tumours, Nat. Rev. Mater. 1 (2016) 1–12.
[37] Q.H. Feng, Y.Y. Zhang, W.X. Zhang, X.N. Shan, Y.J. Yuan, H.L. Zhang, et al., Tumor-targeted and multi-stimuli responsive drug delivery system for near-infrared light induced chemo-phototherapy and photoacoustic tomography, Acta Biomater. 38 (2016) 129–142.
[38] M. Longmire, P.L. Choyke, H. Kobayashi, Clearance properties of nano-sized particles and molecules as imaging agents: considerations and caveats, Nanomedicine 3 (2008) 703–717.
[39] S.H. Tang, M. Chen, N.F. Zheng, Sub-10-nm pd nanosheets with renal clearance for efficient near-infrared photothermal cancer therapy, Small 10 (2014)

3139–3144.
[40] A.J. Trinidad, S.J. Hong, Q. Peng, S.J. Madsen, H. Hirschberg, Combined concurrent photodynamic and gold nanoshell loaded macrophage-mediated photothermal therapies: an in vitro study on squamous cell head and neck carcinoma, Lasers Surg. Med. 46 (2014) 310–318.
[41] Y. Cheng, Q. Dai, R.A. Morshed, X. Fan, M.L. Wegscheid, D.A. Wainwright, et al., Blood-brain barrier permeable gold nanoparticles: an efficient delivery platform for enhanced malignant glioma therapy and imaging, Small 10 (2014) 5137–5150.
[42] C. Engblom, C. Pfirschke, M.J. Pittet, The role of myeloid cell in cancer therapies, Nat. Rev. Cancer 16 (2016) 447–462.
[43] S.J. Madsen, S.K. Baek, A.R. Makkouk, T. Krasieva, H. Hirschberg, Macrophages as cell-based delivery systems for nanoshells in photothermal therapy, Ann. Biomed. Eng. 40 (2012) 507–515.
[44] R. Mooney, L. Roma, D. Zhao, D. Van Haute, E. Garcia, S.U. Kim, et al., Neural stem cell-mediated intratumoral delivery of gold nanorods improves photothermal therapy, ACS Nano 8 (2014) 12450–12460.
[45] Y. Yang, J. Zhang, F. Xia, C. Zhang, Q. Qian, X. Zhi, et al., Human CIK cells loaded with Au nanorods as a theranostic platform for targeted photoacoustic imaging and enhanced immunotherapy and photothermal therapy, Nanoscale Res. Lett. 11 (2016) 285.
[46] Y. Liu, M. Yang, J. Zhang, X. Zhi, C. Li, C. Zhang, et al., Human induced pluripotent stem cells for tumor targeted delivery of gold nanorods and enhanced photothermal therapy, ACS Nano 10 (2016) 2375–2385.
[47] L. Li, Y. Guan, H. Liu, N. Hao, T. Liu, X. Meng, et al., Silica nanorattle-doxorubicin-anchored mesenchymal stem cells for tumor-tropic therapy, ACS Nano 5 (2011) 7462–7470.
[48] D.F. Quail, J.A. Joyce, Microenvironmental regulation of tumor progression and metastasis, Nat. Med. 19 (2013) 1423–1437.
[49] S.K. Patel, J.M. Janjic, Macrophage targeted theranostics as personalized nanomedicine strategies for inflammatory diseases, Theranostics 5 (2015) 150–172.
[50] M.R. Choi, K.J. Stanton-Maxey, J.K. Stanley, C.S. Levin, R. Bardhan, D. Akin, et al., A cellular Trojan Horse for delivery of therapeutic nanoparticles into tumors, Nano Lett. 7 (2007) 3759–3765.
[51] C. Murdoch, A. Giannoudis, C.E. Lewis, Mechanisms regulating the recruitment of macrophages into hypoxic areas of tumors and other ischemic tissues, Blood 104 (2004) 2224–2234.
[52] Z.B. Li, H. Huang, S.Y. Tang, Y. Li, X.F. Yu, H.Y. Wang, et al., Small gold nanorods laden macrophages for enhanced tumor coverage in photothermal therapy, Biomaterials 74 (2016) 144–154.
[53] O. Rabin, P.J. Manuel, J. Grimm, G. Wojtkiewicz, R. Weissleder, An X-ray computed tomography imaging agent based on long-circulating bismuth sulphide nanoparticles, Nat. Mater. 5 (2006) 118–122.
[54] L. Cheng, S.D. Shen, S.X. Shi, Y. Yi, X.Y. Wang, G.S. Song, et al., $FeSe_2$-decorated Bi_2Se_3 nanosheets fabricated *via* cation exchange for chelator-free ^{64}Cu-labeling and multimodal image-guided photothermal-radiation therapy, Adv. Funct. Mater. 26 (2016) 2185–2197.
[55] S.G. Wang, X. Li, Y. Chen, X.J. Cai, H.L. Yao, W. Gao, et al., A facile one-pot synthesis of a two-dimensional MoS_2/Bi_2S_3 composite theranostic nanosystem for multi-modality tumor imaging and therapy, Adv. Mater. 27 (2015) 2775–2782.
[56] G. Song, C. Liang, H. Gong, M. Li, X. Zheng, L. Cheng, et al., Core-shell MnSe@Bi_2Se_3 fabricated via a cation exchange method as novel nanotheranostics for multimodal imaging and synergistic thermoradiotherapy, Adv. Mater. 27 (2015) 6110–6117.
[57] G.S. Song, C. Liang, X. Yi, Q. Zhao, L. Cheng, K. Yang, et al., Perfluorocarbon-loaded hollow Bi_2Se_3 nanoparticles for timely supply of oxygen under near-infrared light to enhance the radiotherapy of cancer, Adv. Mater. 28 (2016) 2716–2723.
[58] X.D. Zhang, J. Chen, Y. Min, G.B. Park, X. Shen, S.S. Song, et al., Metabolizable Bi_2Se_3 nanoplates: biodistribution, toxicity, and uses for cancer radiation therapy and imaging, Adv. Funct. Mater. 24 (2014) 1718–1729.
[59] Y. Min, G.D. Moon, B.S. Kim, B. Lim, J.S. Kim, C.Y. Kang, et al., Quick, controlled synthesis of ultrathin Bi_2Se_3 nanodiscs and nanosheets, J. Am. Chem. Soc. 134 (2012) 2872–2875.
[60] A. Zhuang, J.J. Li, Y.C. Wang, X. Wen, Y. Lin, B. Xiang, et al., Screw-dislocation-driven bidirectional spiral growth of Bi_2Se_3 nanoplates, Angew. Chem. Int. Ed. Engl. 53 (2014) 6425–6429.
[61] H. Peng, K. Lai, D. Kong, S. Meister, Y. Chen, X.L. Qi, et al., Aharonov-bohm interference in topological insulator nanoribbons, Nat. Mater. 9 (2010) 225–229.
[62] K.J. Koski, J.J. Cha, B.W. Reed, C.D. Wessells, D. Kong, Y. Cui, High-density chemical intercalation of zero-valent copper into Bi_2Se_3 nanoribbons, J. Am. Chem. Soc. 134 (2012) 7584–7587.
[63] J.J. Fu, D. Wang, D. Mei, H.R. Zhang, Z.Y. Wang, B. He, et al., Macrophage mediated biomimetic delivery system for the treatment of lung metastasis of breast cancer, J. Control Release 204 (2015) 11–19.
[64] L. Milane, S. Ganesh, S. Shah, Z.F. Duan, M. Amiji, Multi-modal strategies for overcoming tumor drug resistance: hypoxia, the Warburg effect, stem cells, and multifunctional nanotechnology, J. Control Release 155 (2011) 237–247.
[65] M. Zhou, J.J. Li, S. Liang, A.K. Sood, D. Liang, C. Li, CuS nanodots with ultrahigh efficient renal clearance for positron emission tomography imaging and image-guided photothermal therapy, ACS Nano 9 (2015) 7085–7096.
[66] P.H. Zhang, C. Wang, J.J. Zhao, A.Q. Xiao, Q. Shen, L.T. Li, et al., Near infrared-guided smart nanocarriers for microRNA-controlled release of doxorubicin/siRNA with intracellular ATP as fuel, ACS Nano 10 (2016) 3637–3647.
[67] K. Yang, J.M. Wan, S. Zhang, Y.J. Zhang, S.T. Lee, Z. Liu, *In vivo* pharmacokinetics, long-term biodistribution, and toxicology of PEGylated graphene in mice, ACS Nano 5 (2011) 516–522.
[68] Z. Li, Y. Hu, K.A. Howard, T. Jiang, X. Fan, Z. Miao, et al., Multifunctional bismuth selenide nanocomposites for antitumor thermo-chemotherapy and imaging, ACS Nano 10 (2016) 984–997.

Supporting Information for

Cell-borne 2D nanomaterials for efficient cancer targeting and photothermal therapy

Zhibin Li [a, b], Jundong Shao [a], Qian Luo [a], Xue-Feng Yu [a, *], Hanhan Xie [a], Haidi Fu [c], Siying Tang [a], Huaiyu Wang [a, *], Guangli Han [c], Paul K. Chu [b, *]

[a] *Institute of Biomedicine and Biotechnology, Shenzhen Institutes of Advanced Technology, Chinese Academy of Sciences, Shenzhen 518055, Guangdong, P. R. China*

[b] *Department of Physics and Materials Science, City University of Hong Kong, Tat Chee Avenue, Kowloon, Hong Kong, China*

[c] *School and Hospital of Stomatology, Wuhan University, 237 Luoyu Road, Wuhan 430079, P. R. China*

*Corresponding authors: Tel: +852-34427724; Fax: +852-34420542 (P.K. Chu)

E-mail addresses: xf.yu@siat.ac.cn (X. -F. Yu); hy.wang1@siat.ac.cn (H. Y. Wang); paul.chu@cityu.edu.hk (P. K. Chu)

Keywords: 2D nanomaterials, Bi_2Se_3 nanosheets, near-infrared, drug delivery, photothermal therapy

Table S1. Elemental composition of Bi_2Se_3 nanosheets determined by ICP-OES.

Samples	Bi (μmol/L)	Se (μmol/L)	Bi/Se atom ratio
1	0.933	1.406	0.664
2	2.646	3.964	0.668
3	8.221	12.361	0.665

Table S2. Pharmacokinetics data of Bi and Se for Bi_2Se_3-laden-macrophages and Bi_2Se_3 nanosheets after intravenous injection into BALB/c mice.

Parameter	Bi element		Se element	
	Bi_2Se_3-laden-macrophages	Bi_2Se_3	Bi_2Se_3-laden-macrophages	Bi_2Se_3
$t_{1/2}\alpha$ (h)	0.84 ± 0.01	0.34 ± 0.02	0.72 ± 0.03	0.56 ± 0.02
$t_{1/2}\beta$ (h)	15.58 ± 1.90	6.42 ± 1.50	8.50 ± 1.56	7.28 ± 2.99
$AUC_{0\text{-}25\ days}$ (μg/mL*h)	669.00 ± 93.01	331.41 ± 77.33	258.32 ± 52.81	95.11 ± 44.58
CL_1 (mL/h)	0.26 ± 0.05	1.26 ± 1.10	0.58 ± 0.15	1.96 ± 1.19
CL_2 (mL/h)	1.51 ± 0.79	2.91 ± 0.55	1.40 ± 0.12	3.08 ± 0.34

Abbreviations: $t_{1/2}\alpha$: blood distribution half-life; $t_{1/2}\beta$: blood terminal elimination half-life; $AUC_{0\text{-}25\ days}$: area under the concentration-time curve from 0 to 25 days; CL_1: center compartment clearance; CL_2: the peripheral compartment clearance.

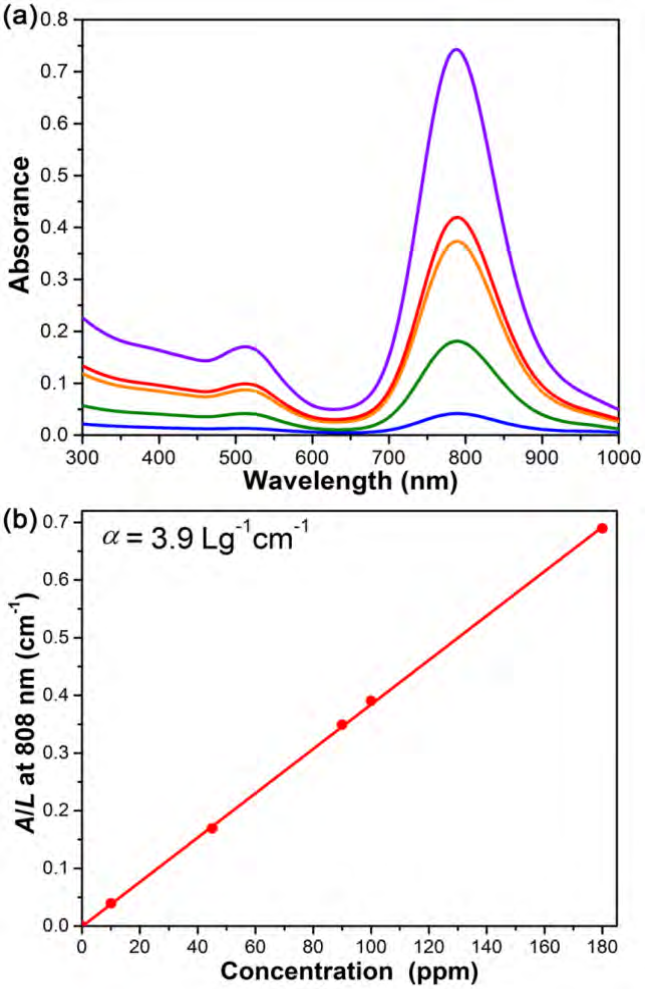

Fig. S1. (a) Absorbance spectra for different concentrations of Au nanorods in aqueous solutions. The top curve is 22.0 ppm and each subsequent curve is diluted 1:2; (b) Fitted line of normalized absorbance intensity over the characteristic cell length (*A/L*) versus concentrations.

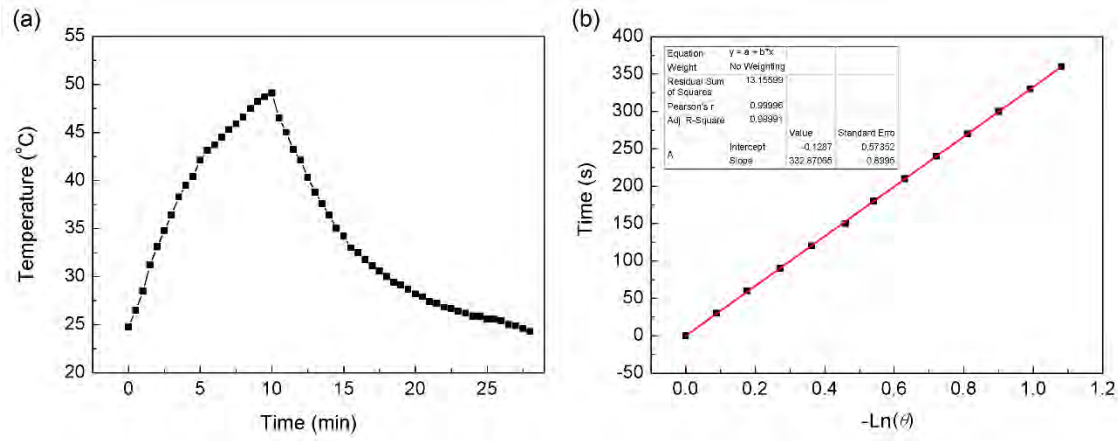

Fig. S2. (a) Photothermal effect of the aqueous dispersion of Bi_2Se_3 nanosheets under NIR laser (808 nm, 1.0 W/cm^2) irradiation for 10 min before the laser is turned off. (b) Time constant for heat transfer from the system is determined to be τ_S = 333 s by applying the linear time data from the cooling period versus negative natural logarithm of driving force temperature, which is obtained from the cooling stage of panel. The photothermal conversion efficiency (η) can be calculated by Eqs. (1-4) [1,2]

$$\eta = (hS(T_{max}-T_{surr})-Q_{dis})/I(1-10^{-A}) \quad (1)$$

$$hS = \sum mC_p/\tau_S \quad (2)$$

$$\tau_S = -t/\ln\theta \quad (3)$$

$$\theta = (T - T_{surr})/(T_{max} - T_{surr}) \quad (4)$$

where h is the heat transfer coefficient, S is the surface area of the container, τ_S is the time constant for heat transfer from the system, m is mass of products (m = 1 g), C_p is specific heat capacity of solvent (C_p, water = 4.2 Jg^{-1}°C^{-1}), and τ_S = 333 s is obtained from the following Figure. Q_{dis} is measured independently to be 174.5 mW, hS is obtained from Eqs(2) (hS = 1*4.2/333= 12.6 mW/°C), T_{max} is the equilibrium temperature of Bi_2Se_3 nanosheets, T_{surr} is the ambient temperature of the surroundings, I is the laser power density (1.0 W/cm^2), and A is the absorbance of Bi_2Se_3 nanosheets at 808 nm (A_{808} = 0.3). Accordingly, η = {[12.6*(49.1-24.8)-174.5]/[1000*(1-10$^{-0.3}$)]}*100%= 26.4%.

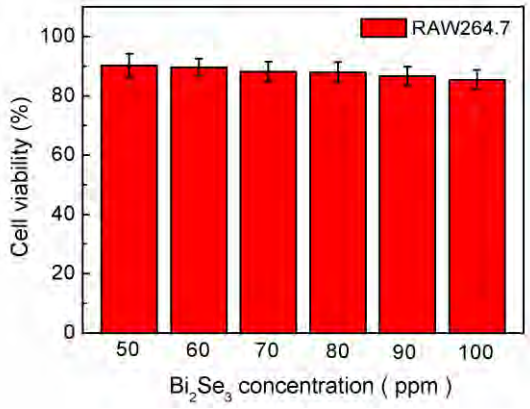

Fig. S3. Cell viability of RAW264.7 cells incubated with large concentrations of Bi_2Se_3 nanosheets for 24 h.

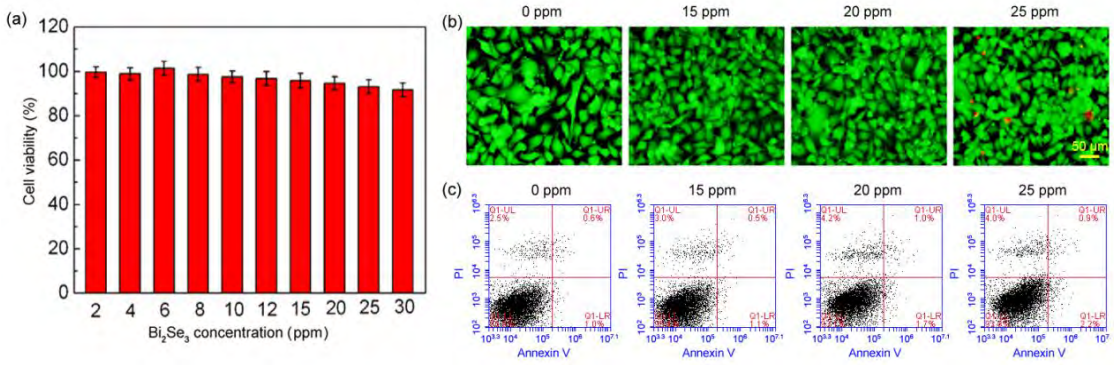

Fig. S4. Cytocompatibility of the Bi_2Se_3 nanosheets with MCF-7 cells: (a) MTT assay; (b) Calcein AM/PI staining (viable cells can be green-stained with Calcein AM with dead cells stained red with PI); (c) Flow cytometric results.

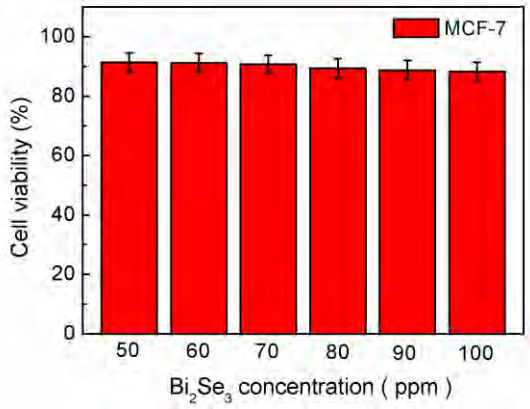

Fig. S5. Cell viability of MCF-7 cells incubated with high concentrations of Bi_2Se_3 nanosheets for 24 h.

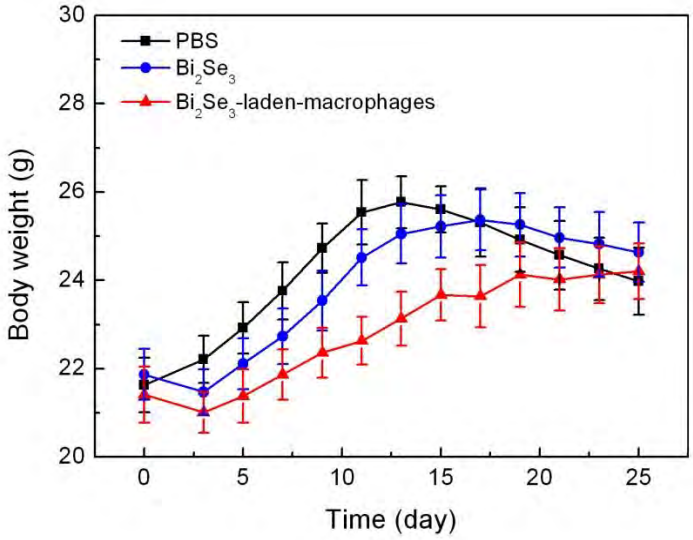

Fig. S6. Body weight curves of the MCF-7 tumor-bearing mice in each group after photothermal therapy.

References:

[1] Q. Tian, F. Jiang, R. Zou, Q. Liu, Z. Chen, M. Zhu, et al., Hydrophilic Cu_9S_5 nanocrystals: a photothermal agent with a 25.7% heat conversion efficiency for photothermal ablation of cancer cells *in vivo*, ACS Nano 5 (2011) 9761-9771.

[2] D.K. Roper, W. Ahn, M. Hoepfner, Microscale heat transfer transduced by surface plasmon resonant gold nanoparticles, J. Phys. Chem. C. Nanomater Interfaces 111 (2007) 3636-3641.